Conceptual Design of a Counter-Rotating Fan System for Distributed Boundary Layer Ingesting Propulsion

B.J.Lee[1], May-Fun Liou[2], and M. Celestina[2]

Vantage Partners, LLC[1]
NASA Glenn Research Center[2]
Aero-propulsion Division
Cleveland
USA

ABSTRACT

The present paper details the design of counter rotating fans for a Turboelectric Distributed Propulsion (TeDP) system. Sixteen propulsors installed are embedded on an aerodynamically optimized hybrid wing-body configuration in mail-slot-shape nacelles. The hybrid wing-body configuration which was previously designed to satisfy the conditions of trim, longitudinally static stability and specific cargo space is employed as the influencing body configuration in pursuing an optimal distributed propulsion system. A counter-rotating fan system for the distributed propulsors is conceptually designed and the performance is evaluated against the target thrust mandated by the mission requirements. The concept of the distributed propulsion allows the fan pressure ratio to be around 1.30 to achieve the target thrust. In addition, further splitting of the fan pressure ratio by using the counter-rotating fans for each slot realizes the target pressure ratio with low tip speed. Aerodynamic shape optimizations of the fan blades are performed in a sequential multi-objective optimization process for various design objectives, such as mass flow rate condition, fan pressure ratio, efficiency and the exit flow angle of the fan stage by using a genetic algorithm, NSGA-II. The radial chord distribution, and meanline distribution of the rotors are designed on the circumferentially averaged axisymmetric inlet profiles and tested on the profiles from six divided sectors to reckon the flow distortion. The performances of the counter rotating fans are, thus, evaluated and compared with a conventional high-speed fan accordingly to find distortion tolerant characteristics of the present concept.

Keywords: Boundary Layer Ingestion, Hybrid Wing/body, Turbo-machinery, Aerodynamic Conceptual Design, Distributed Electric Propulsion, Counter Rotating fans

NOMENCLATURE

ADP	aerodynamic design point
AOA	angle of attack
AIP	aerodynamic interface plane
BLI	boundary layer ingestion
CRFs	counter rotation fan system
FPR	fan pressure ratio
FSPR	fan stage pressure ratio
HWB	hybrid wing-body
IMM	immersion index
ISA	international standard atmosphere
M	mach number
$\dot{m}$	mass flow rate
N	physical rotational speed (in RPM)
N_c	corrected rotational speed (in RPM)
Re/m	Reynolds number per meter
PAI	propulsion airframe integration
P_{shaft}	shaft power
P_t	total pressure

p_s static pressure
P_{0i} reference air pressure (e.g. 101.35 kN/m^2, STD)
PR   total pressure ratio
P_p propulsive power
r radius in the cylindrical coordinate
R_1 front rotor
R_2 rear rotor
Th_0 target thrust
T_s static temperature
T_t total temperature
U   rotational velocity of the blade (rω)
W_m meridional velocity
W_c corrected mass flow rate
ρ   density
η_{ad} adiabatic efficiency
η_{poly} polytropic efficiency
φ pressure ratio of the front and after rotors
α flow swirl angle in absolute frame
β flow swirl angle in relative frame
ω   rotational angular velocity

Subscript
1   property of the front rotor
2   property of the rear rotor
∞   free stream condition
c   corrected
f   fan
goal   target property for design
e   exit
h   hub
s   shroud (tip)

1.0   INTRODUCTION

A hybrid wing-body (HWB) concept is being considered by NASA as a potential subsonic transport aircraft that meets aerodynamic, fuel, emission, and noise goals in the time frame beyond 2050. While the concept promises advantages over the conventional wing-and-tube aircraft, it poses unknowns and risks, and thus requires in-depth and broad assessments. Specifically, the configuration entails a tight integration of the airframe and propulsion geometries; the aerodynamic impact should be carefully evaluated. This realization has led to several studies and research efforts in the past, including a system analysis[1] of a baseline design of the N3-X, high-fidelity flow simulations to understand the effects of the propulsion-airframe integration (PAI) on the flow and later aerodynamic redesign through optimization techniques.[2-6] Among those efforts, HWB has been dealt in three aspects: airframe with nacelle, propulsor with flow-path, and PAI with stability. On the airframe with nacelle side, the Class function/Shape function Transformation which is a CAD (Computer-Aided Design) and non-dimensional airfoil/wing generation method, was adopted to effectively construct the HWB airframe-propulsion configuration.[2] The parameterization method enables a PAI design approach that considered both the airframe and propulsion system together at the outset of the aerodynamic design of the aircraft. Furthermore, the nacelle cowl shape was designed and optimized using adjoint method to improve aerodynamic performance of the nacelle.[3] On the propulsion side, a numerically efficient body force model was introduced to incorporate the effects of turning and flow loss from the fan stage[4,5] to make the PAI optimization computationally feasible.

Recently, aerodynamic shape design and optimization were performed to determine geometric shape parameters by minimizing the drag while was subjected to the lift, pitching moment, and cargo capacity constraints.[6] Thus, a conceptual configuration of the N3-X aircraft for 300-passenger-seats was designed and named N3X-Dep300 (Dep:

distributed electric propulsion). The latest work resolved the challenges against minimal drag with fixed lift, being longitudinally static stable, trimmable with a physical cargo space. However, the ducted propulsor was simply modeled by an assumption of a uniform back pressure boundary condition at the inlet throat. The accuracy of this 1-D assumption may not be adequate in case highly distorted flow is ingested into the nacelle because the impacts of the radial and circumferential variations of the static pressure were unaccounted for. Thus, an actuator disk model is applied latter to derive an appropriate inlet profile for the propulsion system.[5] Ref. [5] illustrated the expected power saving for the distributed propulsor relative to clean inlet flow engines and derived the target design conditions for the propulsor design in an optimization manner.
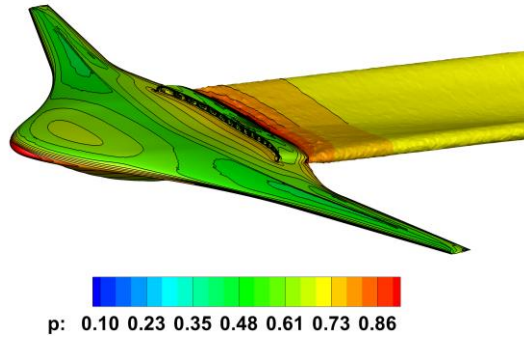

p: 0.10 0.23 0.35 0.48 0.61 0.73 0.86

Figure 1. Previous design of N3X-DEP300[5,6], propulsion airframe integration and jet flow
(pressure iso-surface) from the mail-slot propulsion system
(Cruise Condition: M=0.84, Re= 7.2 million/m, 40kft Altitude, 80kN Thrust generation)

The present study focuses on the conceptual design of its boundary layer tolerant turbo-machinery component built on the bases of the previously reported and described airframe[6] and distributed propulsion system[5] in order to complete the whole PAI configuration as shown in Fig. 1. The biggest concern in designing the embedded propulsor is the impact of the swirl distortion from the incoming boundary layer profile causing significant incidence swing at the fan face. The problem becomes more significant as the rotor tip speed exceeds the sonic speed. As a result of the needs to lower the tip loading and reduce performance deficit from the significant incidence swing to the rotors, the concepts of distributed propulsion system and splitting the loading of each rotor into a pair of counter-rotating fans (CRFs) are adopted in the present design. The design optimization of CRFs are carried out based on turbomachinery CFD analysis[7,8] and a multi-objective evolutionary algorithm.[9]

The present paper consists of 5 chapters hereafter. Chapter 2 will briefly introduce the design requirements, inlet profile and design strategies of the CRFs. Chapter 3 will discuss the vector diagram of the fan design to determine the speed ratio and constraints in the current study. Chapter 4 is going to discuss about the optimization results and the comparisons between designs for axisymmetric and non-axisymmetric inlet profile, then followed by chapter 5 that will detail the overall propulsor performance compared with a conventional high-speed fan and the advantages from the current conceptual propulsor design.

2.0   DESIGN STRATEGY

2.1   System Design Requirements

The thrust requirements for each flight condition from the original N3-X system design[1] are provided in table 1. The propulsor design are focused on the cruise condition at the altitude of 40,000 feet. The minimum thrust requirement is 74kN based on the clean wing aircraft. The figure 2 shows the thrust–shaft power curve of the N3x-DEP300 compared with a clean inlet propulsor and the original system design at the condition. It is observed that each slot shows different thrust-shaft power curve and power saving relative to the clean inlet propulsor depending on the amount of the ingested boundary layer. The model applied to obtain the curves is actuator disk model of which fan stage pressure ratio is 1.28~1.31 and stage adiabatic efficiency is 88%. However, the modeling in the original system design assumed that the fan pressure ratio is 1.30, adiabatic

efficiency is 93.5% with 1% distortion penalty. Hence, shaft power requirement for the 4.6kN thrust shows about 20~25% discrepancy between system design goal and CFD analysis per slot.

The disconnect between the state-of-art CFD analyses and the goal from the system design stems from couple of reasons. One of the critical reasons is that there are not sufficiently accumulated experience through the propulsor performance test under a significant circumferential inlet distortion that supports the system level design of BLI aircrafts. Another is immature technology for inlet/fan analysis and designs. The only propulsor test which considered the boundary layer ingestion and the interaction of inlet/fan stage is BLI2DTF test.[10] The configuration is tested for FSPR=1.34 and achieved 87.9% adiabatic efficiency throughout the fan stage at ADP. Thus, the technology level related to the distortion tolerant fan design still shows a substantial gap from the required technology level beyond 2050s.

Table 1. Design Requirements [J. Felder et al.[1]]

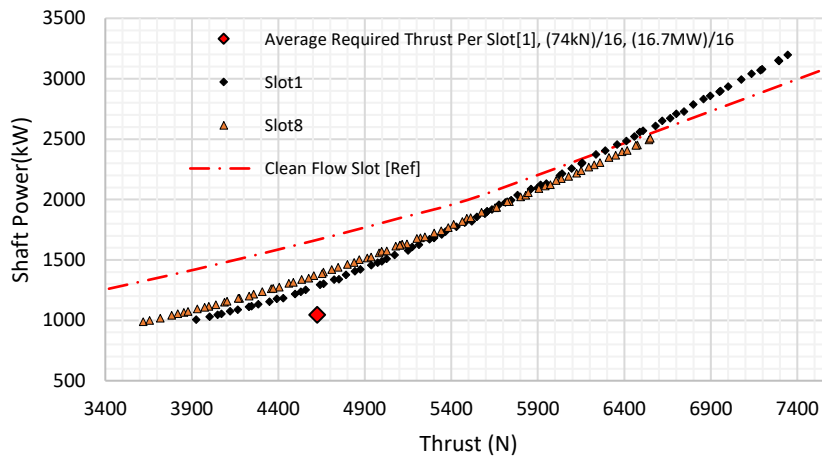| Flight Conditions	Minimum Thrust Requirement	MFR
ADP(30kft/0.84/ISA)	26,750 lbf (118.98kN)	2788 lbm/sec (1265kg/sec)
Cruise (40kft/0.84/ISA)	16,656 lbf (74kN)	1785 lbm/sec (810kg/sec)
Rolling Take-Off (RTO) (SL/0.25/ISA+27R)	65,000 lbf	5368 lbm/sec
Sea Level Static Take-Off(T/O) (SL/0.0/ISA)	90,000 lbf	5745 lbm/sec

Figure 2. Shaft power comparison relative to the thrust from the baseline configuration at cruise condition (40kft/0.84/ISA). [5]

The present conceptual design work is intended to mitigate the gap by changing the concept of the propulsor system which enables higher propulsor efficiency in a distorted inlet flow condition and seek after a bottom-up feedback from the propulsor module design to other modules such as inlet/airframe as well as to the system level design by using higher fidelity analysis and design methods. The target conditions are the thrust requirement of 80kN, the fan stage pressure ratio of 1.31 with a mass flow rate, $\dot{m} = 56$kg/sec (Corrected mass flow rate: W_c=128.7kg/sec, STD), minimum stage efficiency requirement for 88% at 40k feet altitude. The condition corresponds to the design conditions of the inner board slots of N3x-DEP300 configuration.[5] If the design goal is achieved, the shaft power requirement of the BLI propulsor will be about 24MW for the whole aircraft at 80kN thrust while the clean inlet engine requires about 29MW. Thus, the shaft power requirement of the embedded configuration would be expected to be 20% less than what the conventional clean inlet flow engine configuration requires.[5]

2.2   Inlet Profiles & Turbo-machinery Design Conditions

Figures 3 schematically depict the flow-path, computational domain and important stations indexed relative to the rotor positions within a single mail-slot. Total 16 propulsors are located on the upper surface of the fuselage along the trailing edge to maximize the ingestion of wake[12] from the influencing body as shown in Figs. 4. The specifications of the rotors are provided in Table 2. The flow-path originates from R4[4,13] fan hub and shroud shapes, thus, the specification of the front rotor is following R4 rotor and the rear rotor is based on the OGV flow-path but appropriately modified to accommodate a rotor in the provided flow-path. A better performance, especially to accommodate rear rotor's flow capacity and diffusion factor, could be obtained with a re-design of the flow-path but those consideration can be left for a detailed design of the flow-path with inlet and nozzle. The radial chord profile will be adjusted for a slower rotor tip speed with the mass-flow rate requirement. Thus, the final performance of the optimized CRFs will be compared with that of R4 fan under the same inlet profile conditions.

Table 2. Geometric Specification of the Baseline Rotors

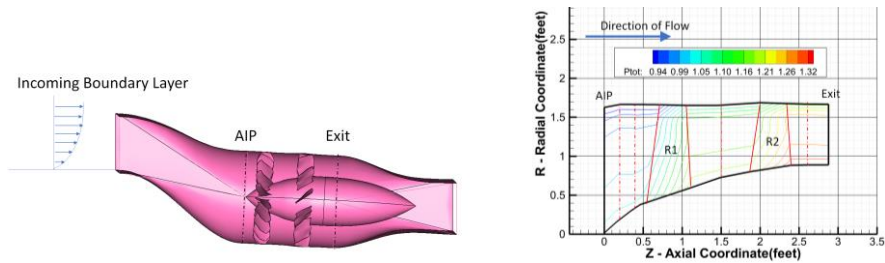|	AR	TR	Hub to Tip Ratio	Fan Diameter (m)
Front Rotor	2.35	0.53	0.22	1.023
Rear Rotor	1.98	0.62	0.47	1.036

Figure 3. Flow-path shape in one mail-slot (left) and computational domain (right) of the turbo-machinery analysis and design. The blue arrow indicates the flow direction.
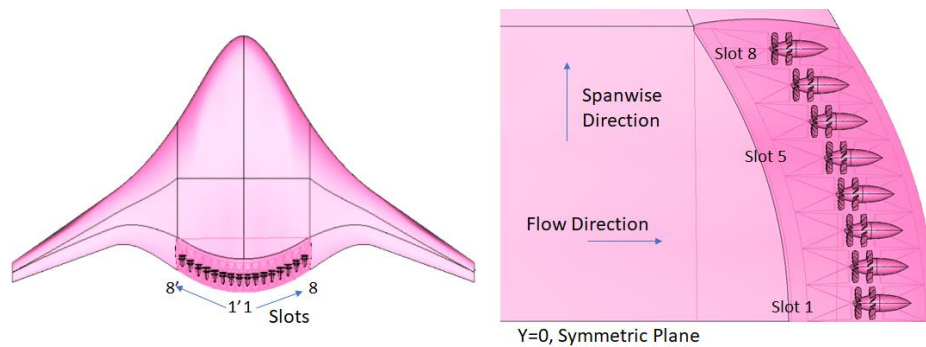

Figure 4. Planform of airframe and locations of mail-slots which are numbered from the root to the outboard.

The inlet profile of each slot is obtained from previous CFD solutions[5] of the N3x-DEP300 PAI configuration as shown in Figs. 5. From the symmetric plane of the planform of the airframe as indicated in Fig. 4, slot index starts from 1 to 8, and the slots on the other half-span are mirrored relative to the y=0 plane and denoted as 1´ to 8´ for the convenience sake. The amount of the ingested boundary layer is largest into the slot 1 as the incoming boundary layer is generated by the longest airframe chord near the root, and smallest into the slot 8. The total pressure contours for inlet and exit domains are non-dimensionalized by a dynamic head, $\rho_\infty c_\infty^2$.[5]

Figures 5 display the normalized total pressure contours of the sampled slots, 1, 5 and 8, at the aerodynamic interface plane (AIP) and the exit of the fan stage.[5] As shown in all the slots of the figures, the flow field at the AIP is in horizontal layers due to ingested boundary layers at the inlet and slot 8 ingests more clean flow as the boundary layer gets thinner toward the outboard. As a result, the flow pattern at the AIP is shown

circumferentially and radially distorted as expected, hence, non-axisymmetric inflow is predicted at the fan face. After the AD model augment the flow with a 80kN worth energy, much higher total pressure jet flows are observed at the exit of the fan stage.
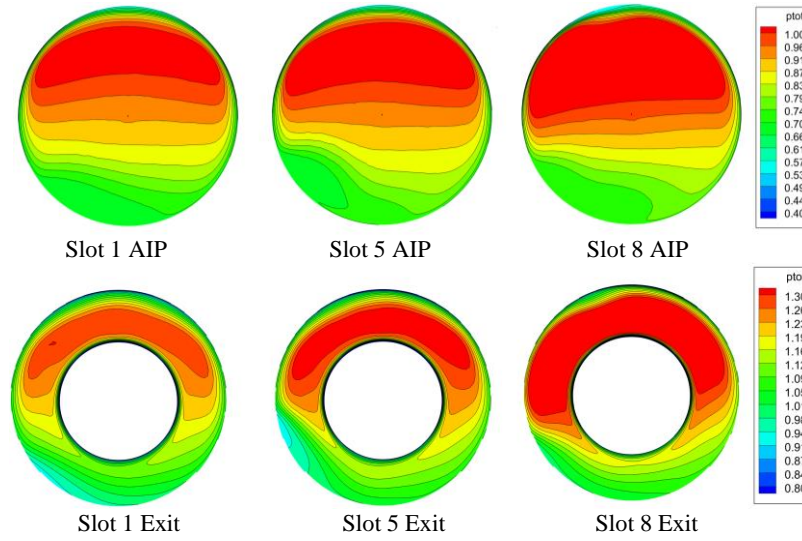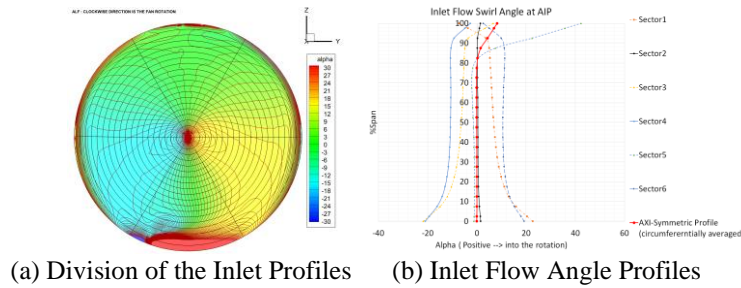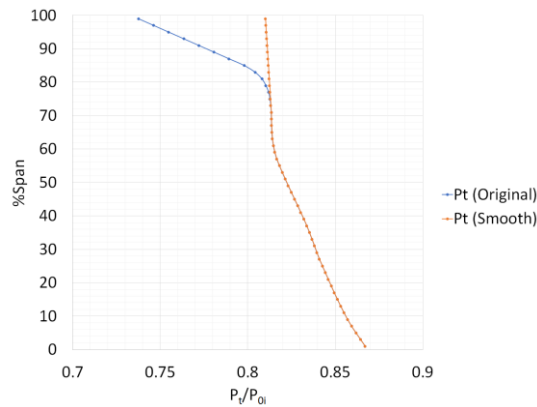

Slot 1 AIP   Slot 5 AIP   Slot 8 AIP

Slot 1 Exit   Slot 5 Exit   Slot 8 Exit

Figure 5. Inlet and Exit profiles of Mail-Slot Propulsors
for the target thrust (80kN) configuration in Ref.[5]

(a) Division of the Inlet Profiles   (b) Inlet Flow Angle Profiles


(c) Total Pressure Profiles of the circumferential averaged axisymmetric inlet profile
Figure 6. Inlet Profiles for the Design Optimization and the Division of Sectors
(AIP location, Slot 1)

The non-axisymmetric inlet profile of the slot 1 in Fig. 6-(a) which ingests most of boundary layer among the slots is adopted as a representative profile for the present design study. The inlet profile is divided into multiple pi-shaped sectors to obtain mass-averaged radial profiles from different circumferential locations. The flow swirl angle profiles are compared with a full-annulus averaged axisymmetric profile in Fig. 6-(b). The observed swing in the absolute flow angle (α) is about $\pm 10°$ at the mid-span, and $\pm 20°$ at the hub respectively. Note that the swing in the flow angle is measured at AIP station, the amplitude of the swing will be mitigated as the flow-path converges toward the fan

face. The separation from the S-shaped duct causes a singular point of the incidence (swing up to +40° from -5°) at the tip in sector 5. Even though the separated incoming flow is confined in a local region and it is believed that the singularity characteristics of the sector 5 tip could be reduced by the further refinement in the inlet design, the effect of the profile at 80~100%span in the sector 5 is removed in the averaged axisymmetric design profile as shown in Fig. 6-(c), while the performance check will be carried out for the sectorial profile.
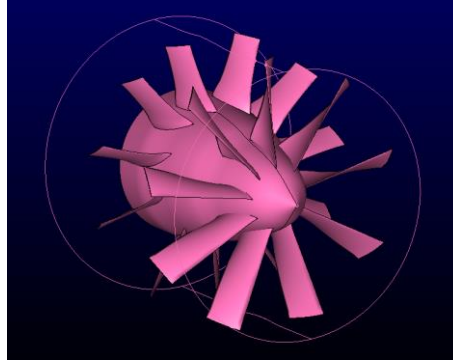
(a) CRFs Geometry Output from the BLADELTE V1.0 (Example)
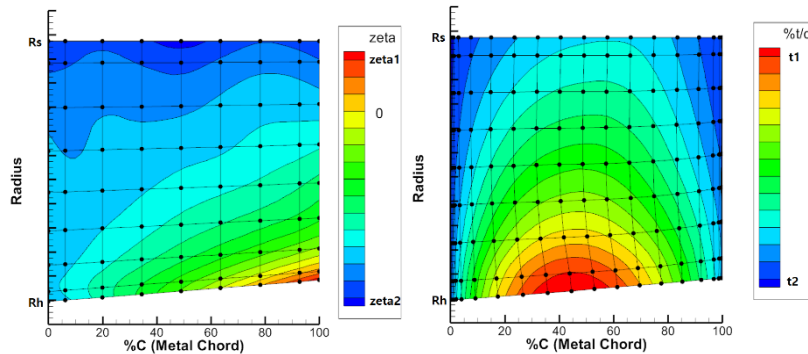
(b) Meanline Parameters (Example) (c) Thickness Parameters (Example)
Figure 7. Blade Design Outputs and Control Points for the Design Parameters

2.3   Geometric Representation of Blades

The blade geometries are generated using BLADELTE v1.0[7] which is a NASA's in-house turbo-machinery geometric design tool. The 3-D blade shape is represented by the meanline, thickness distributions in the chord-wise and radial directions, and radial chord distribution. Those design parameters are represented by a B-spline surface and re-stacked along the provided stacking axis. If the stacking axis is not provided, the default option of the rotor stacking is performed based on the sectional CG point which is calculated along each streamline defined in the meridional planes. At the current stage of a conceptual aerodynamic design of the CRFs, the default option is applied throughout all the design processes.

A detailed design should be followed by including thickness variables to realize further distortion tolerance capability. However, the scope of the current study will stop at the demonstration of the capability of overcoming the circumferential distortion using CRFs. In other words, the planform and meanline shaping of a pair of low pressure/low speed counter rotating fans will be designed with axisymmetric profiles and be analysed in the off-design profiles from the divided sectors to account for the penalty against the high level incoming circumferential distortion. A total of 25 meanline variables and 5 chord variables, i.e. 5 meanline and 1 chord variables per each blade section, defined in 5 streamlines are used. The tip clearances of the rotors are ignored during the current conceptual design.

2.4   Quasi-2D Meanline Analysis

The initial blade geometries are obtained from a quasi-2D meanline code[14]. The initial rotational speed of the front rotor and the speed ratio between the rotors are found from

the velocity vector study that will be discussed in Chapter 3. The initial blade angles at the leading and trailing edges are generated via the quasi-2D meanline code analysis for each design condition as explained in Ref.[14]. The axi-symmetric inlet profiles from section 2.2 are applied. The rotational speed of both rotors are constrained by the rotor tip Mach number below 0.7, so that the flow through the CRF system does not experience any significant shock loss. Hence, the corrected rotational speed of the front rotor is limited below 4800RPM and the speed of the rear rotor is defined according to the speed ratio relationship in Eq. (10) which will be introduced in Chaper 3. An example of FSPR=1.31 of the correlation of the rotaitional speed ratio and the split of the pressure ratios between the rotors is presented in Fig. 8. The target polytropic efficiency of both the rotors are assumed to be same as 93% during the meanline analyses.
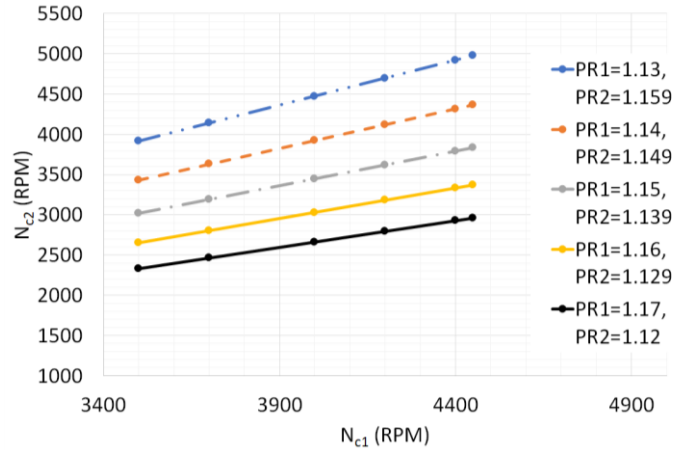

Figure 8. Splitting Pressure Ratio and Corrected Speed for CRFs. (FSPR =1.31)

The quasi-2D meanline code analyzed the conditions in the figure to find out the feasible range of initial design condition that matches the flow capacities of the front and rear rotors as shown in Fig. 9. The flow capacities of the rotors are observed to match with each other between PR_1=1.15 and 1.16 for the target FSPR. In addition, the range of the blade counts are found based on the calculated diffusion factor that is constrained under 0.5. Hence, the minimum numbers of blades for the front and rear stages are 9 and 11 respectively. The rear rotor seems to have tighter design space due to the constraints of the exit flow angle, flow capacity as well as diffusion factor. Consequently, the optimization of the front rotor in the following chapters are carried out for the target pressure ratio of PR=1.15 under the corrected speeds between 4000RPM and 4800RPM, while the rear rotor optimization is performed for the target exit flow angle at the corrected speed ranging from 3000RPM to 4400RPM.
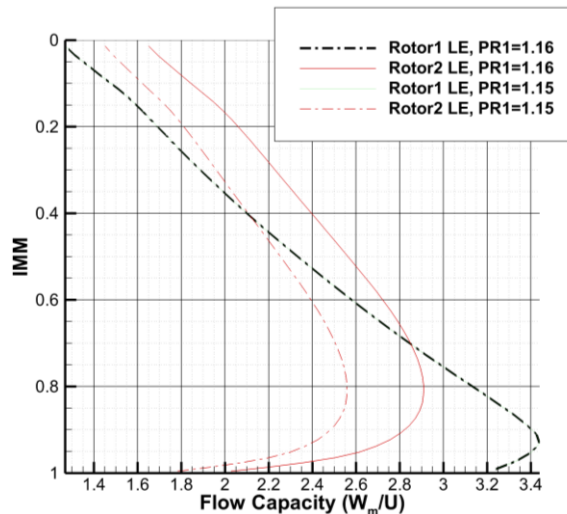

Figure 9. Matching Flow Capacity of the CRFs. [IMM: Immersion (1-%span/100), W_m: Meridional Velocity, U: Rotational Velocity of the blade (rω)]

2.5   Design & Optimization Strategies

Design optimization is carried out for the target design conditions using a single blade row turbo-machinery CFD model and the NSGA-II[9], a multi-objective genetic algorithm. Even in axisymmetric inlet profiles, the radially distorted pressure and angle profiles from the BLI cause a significant efficiency penalty and unsteadiness.[7] Thus, the multi-stage CFD that requires human intervention in finding converged solutions prevents a fully automatic optimization process. Consequently, a sequential design process with a single blade row CFD model is applied to optimize the CRF systems and the performance is evaluated by the multi-stage CFD models as the flow chart shows in Fig. 10.

First, the operating conditions are optimized using DOE and actuator disk models on PAI CFD models to maximize the power saving from the distributed propulsion system as described in Ref. [5]. The PAI model provides inlet profiles and operating conditions for each individual slot. The axisymmetric inlet profile is obtained from the provided non-axisymmetric profile via circumferential mass-weighted average. The axisymmetric profiles are applied to the quasi-2D[14] model to search for an adequate range of the rotational speed of the counter rotating fans by taking the diffusion factors and flow capacity of the rotors into consideration. The quasi-2D model also calculates velocity vectors, a feasible split of the pressure ratio, and the speed ratio. It generates the blade metal angles of the leading and trailing edges as well.
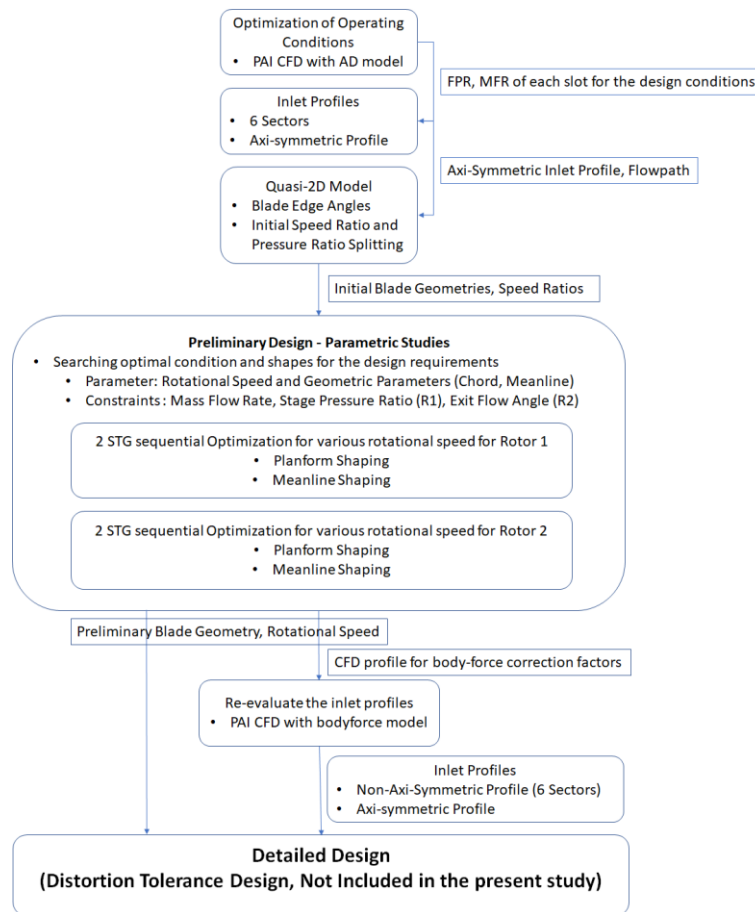

Figure 10. Flowchart of the Conceptual Optimal Propulsor Design

Preliminary optimizations on planform and meanline shapes of the blades are sequentially performed in the order of stages 1 and 2. The stage 2 rotor design uses the exit profile of the optimized stage 1 rotor as the inlet profile for multiple speed ratios within the above-described corrected speed range. The optimal rotational speed, speed ratio and multiple pairs of preliminary blade designs are then obtained. Since the AD model shows different work profile from actually optimized blade pairs, body-force

models that represent the preliminary design are constructed and PAI CFD model is analysed to refine the inlet profiles physically more correct.

The axisymmetric inlet profile and the non-axisymmetric profiles from the 6 sectors from the new PAI CFD model are applied to assess the performance of the preliminary optimal designs. Again, note that detailed design toward the further distortion tolerance is not covered and the scope of the current study is focused on the **optimization of the 'distributed low pressure/low speed counter rotating fans'** and **the demonstration of the distortion tolerance characteristics** of the design concept. Please note that all designs covered in this study are on the basis of PAI perspective.
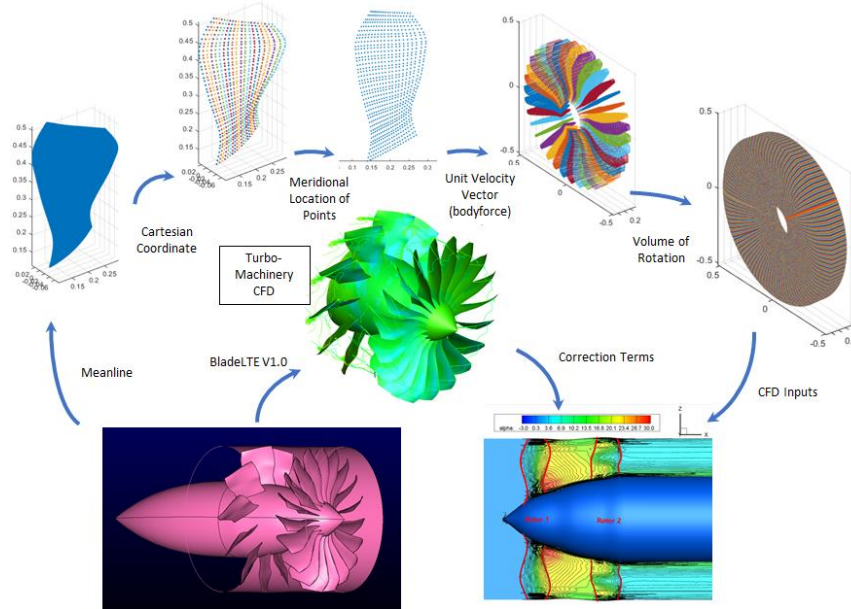

Figure 11. Body-force Modelling Process from BladeLTE.V1.0, and Turbo-machinery CFD analysis. (The contour in FUN3D analysis with body-force is swirl prediction from the counter-rotating fan system in clean inlet flow)

2.6   Body-Force Modeling

Body-force model is known as a numerical strategy to emulate the engine components by adding source terms to the RANS equations. A body-force model[4] proposed by Kim et al. is employed in the present study. A significant feature of the model is its capability to match radial profile, efficiency and pressure ratio along the speed line through the correction terms that is derived from body-fitted turbo-machinery CFD analysis and/or test data. Three correction terms to account for the normal force, mass flow and entropy loss respectively are briefly described as follows. The meanline shape of a blade design is converted to source term input format as shown in Fig. 11. The source term which is calculated by the normal and tangential force components with respect to the blade meanline angles is corrected by radially distributed normal force correction terms. Also the mass flow correction term could be driven by the shape of the speed line. The entropy loss curve from turbo-machinery CFD or test data is applied to get the loss correction in the body-force model. The procedures involved in deriving the body-force model are illustrated in Fig.11. A turbomachinery CFD code runs multi-stage simulation of the designed rotors and provides the required data to the body-force model implemented in a custom version of the FUN3D code for PAI modeling. Meanwhile FUN3D provides the inlet profiles to the turbomachinery CFD model. Data feeding between these two models thus goes on several iterations until their exit flow fields match within a specified tolerance. Figure 12 presents the matched profiles of a set of counter rotating fans at the design corrected speed under clean inlet flow condition. A three-dimensional multi-stage Turbo-machinery CFD model using mixing plane method, SWIFT[8], is employed as shown in Fig. 11.
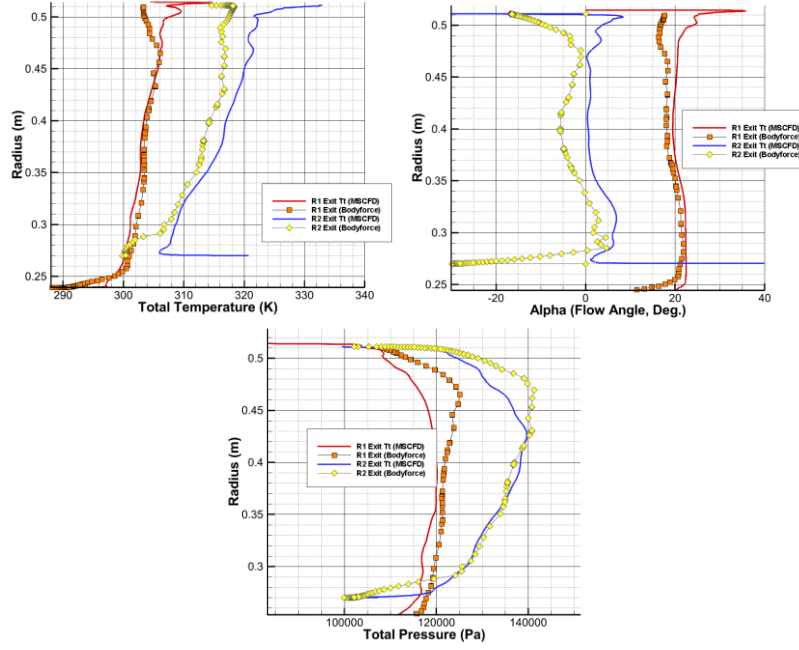
Figure 12. Body-force Profile Matched with the Multi-Stage analyses from the turbomachinery solver SWIFT v4.0, Counter Rotating Fan in a clean inlet flow [N_c=4200/4159RPM, W_c=155.2 kg/sec, STG PR=1.35]

3.0   VELOCITY VECTOR STUDY

In the counter rotating fan design, one of the most critical decisions to be made is finding out an optimal splitting of the fan pressure ratio and speed ratio between two rotors. In general, the rear rotor experiences high diffusion factor and/or is lacking in flow capacity because the inlet relative flow angle (β) is excessively high as shown in the velocity vector diagram in Fig.13. The second rotor is also constrained by the need to turn the flow swirl angle (α_{goal}) back to near zero degree at the exit for maximizing the axial momentum from the propulsor. As a result, this flow angle constraint at the exit of the counter rotating fan provides a very useful correlation of the distribution of the fan pressure ratio between rotors.

The turning force, F_U, in the tangential direction,

$$F_U = \frac{d(mC_U)}{dt} = \dot{m}(dC_U) = \dot{m}(\Delta C_U) = \dot{m}(C_{U2} - C_{U1}) \qquad (1)$$

where, C_U denotes the circumferential velocity in absolute frame for stations 1, 2, 3 and 4 that correspond the LE, TE of the front and rear rotors, respectively. t depicts the physical time.

The torque, T_U is,

$$T_U = \frac{d(mrC_U)}{dt} = \dot{m}(d(rC_U)) = \dot{m}(\Delta(rC_U)) = \dot{m}(r_2 C_{U2} - r_1 C_{U1}), \qquad (2)$$

where, r represents the radii of each location in the corresponding station and $\dot{m}$ denotes the mass flow rate.

similarly, the shaft power P_{shaft} is

$$P_{shaft} = \dot{m}\omega(r_2 C_{U2} - r_1 C_{U1}) = \dot{m}(U_2 C_{U2} - U_1 C_{U1}). \qquad (3)$$

And the work done by the front rotor is

$$W_{k_{rotor}} = \omega(r_2 C_{U2} - r_1 C_{U1}) = r_2 \omega_1 C_{z2} \tan \alpha_2 - r_1 \omega_1 C_{z1} \tan \alpha_1 \qquad (4)$$

Here, C_z is axial velocity for each station and α depicts the flow swirl angle on the

The pressure ratios of the front (φ_1) and rear (φ_2) rotors are,

$$\varphi_1 = \frac{P_{T2}}{P_{T1}} = \left(\frac{T_{T2}}{T_{T1}}\right)^{\frac{\eta_1\gamma}{\gamma-1}} = \left(\frac{H_{T2}}{H_{T1}}\right)^{\frac{\eta_1\gamma}{\gamma-1}} = \left(1 + \frac{U_2 C_{U2} - U_1 C_{U1}}{C_p T_{T1}}\right)^{\frac{\eta_1\gamma}{\gamma-1}} \tag{5}$$

$$\varphi_2 = \frac{P_{T4}}{P_{T3}} = \left(\frac{T_{T4}}{T_{T3}}\right)^{\frac{\eta_2\gamma}{\gamma-1}} = \left(\frac{H_{T4}}{H_{T3}}\right)^{\frac{\eta_2\gamma}{\gamma-1}} = \left(1 + \frac{U_4 C_{U4} + U_3 C_{U3}}{C_p T_{T3}}\right)^{\frac{\eta_2\gamma}{\gamma-1}} \quad , \tag{6}$$

where the polytropic efficiency of each rotor is η_1 and η_2, respectively.
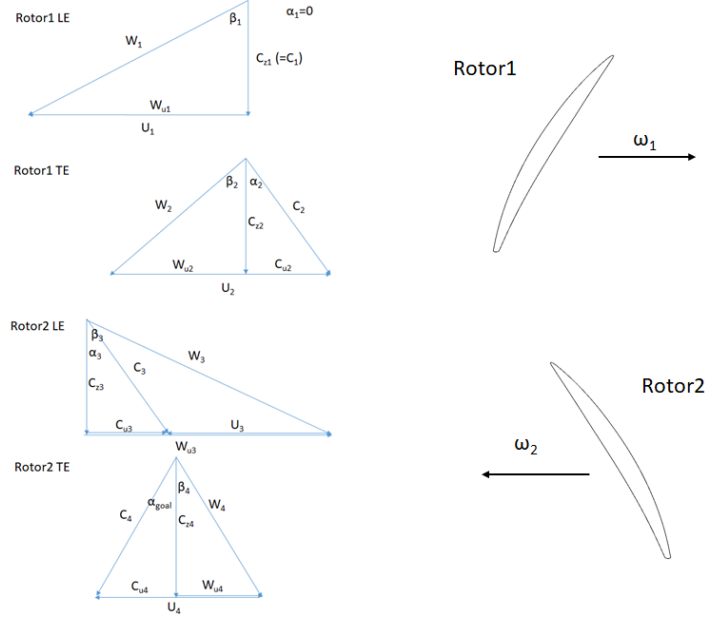

Figure 13. Velocity Vector Diagram for Counter Rotating Fan System and the Station Indices as noted in Fig.3. (W: velocity in relative frame)

Assuming the inlet swirl angle (α_1) being 0°, and no power added into the stream tube contraction between the trailing edge of the front rotor and the leading edge of the rear rotor i.e.,

$$T_{T3} = T_{T2}, \tag{7}$$

equation (4), (5) , and (6) can be further simplified as

$$1 + \frac{r_2\omega_1 C_{z2}\tan\alpha_2}{C_p T_{T1}} = \varphi_1^{\frac{\gamma-1}{\eta_1\gamma}}, \text{ and } \quad 1 + \frac{r_3\omega_2 C_{z3}\tan\alpha_3}{C_p T_{T3}} = \varphi_2^{\frac{\gamma-1}{\eta_2\gamma}} \text{ (only if } sin(\alpha_{goal}) \cong 0) \tag{8}$$

Consequently, the equations (8) will be re-arranged as,

$$\varphi_2^{\frac{\gamma-1}{\eta_2\gamma}} = 1 + \omega_2/\omega_1 \frac{\kappa(\varphi_1^{\frac{\gamma-1}{\eta_1\gamma}}-1)C_p T_{T1}}{C_p T_{T2}}, \quad \text{where } \kappa = \frac{r_3 C_{z3}\tan\alpha_3}{r_2 C_{z2}\tan\alpha_2}. \tag{9}$$

Thus, the rotational speed and pressure ratio of the counter rotating fans can be correlated as follows,

$$\frac{\omega_2}{\omega_1} = \frac{1}{\kappa}\frac{\varphi_2^{(\gamma-1)/(\eta_2\gamma)}-1}{1-\varphi_1^{-(\gamma-1)/(\eta_1\gamma)}} \quad . \tag{10}$$

The κ in the equation (10) depends on the contraction of the flowpath as in Eq.(11)

$$\kappa = \frac{r_3 C_{z3}\tan\alpha_3}{r_2 C_{z2}\tan\alpha_2} = \left(\frac{r_{2,s}^2 - r_{2,h}^2}{r_{3,s}^2 - r_{3,h}^2}\right), \tag{11}$$

obtained from the conservation equations of the mass and angular momentum. Here, the subscripts *s* and *h* denote shroud and hub at each station.

The κ value from the present flowpath between stations 2 and 3 is 1.39. At four efficiency settings, (η_1, η_2), i.e., (0.95, 0.90), (0.90, 0.90), (0.90, 0.83) and (0.96, 0.83), the corresponding speed ratio versus pressure ratio curves for the category 3 (FPR=1.31) design condition are plotted in Fig. 14.
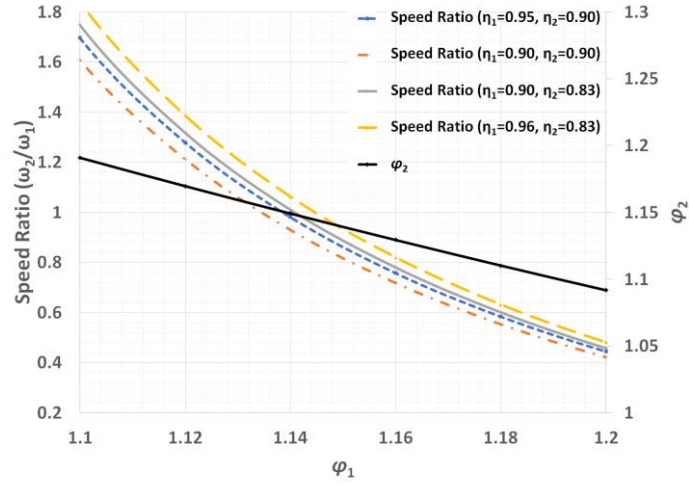

Figure 14. Determination of speed and pressure ratios of counter rotating fans.

In general, the most critical concern in designing counter rotating fans is to match the flow capacity of the two rotors as was discussed in Ch. 2.4. Thus, too excessive hub contraction as like that of a conventional fan-OGV system may cause lack of the flow capacity in the 2nd stage. On the other hand, an open flow-path will increase the diffusion factor of the stage. Thus, an optimal pocket of the speed range of the rear rotor could be obtained by the following considerations for the given flow-path constraints. The diffusion factor of the rotor can be evaluated by equation (12),

$$D_{R2} = 1 - \frac{W_4}{W_3} + \left| \frac{r_4 C_{U4} - r_3 C_{U3}}{(r_4 + r_3)\sigma W_3} \right| \leq D_{max}(\cong 0.5) \tag{12}$$

and it is subjected to a geometric constraint of D_{max}.[15]

4.0   DESIGN OPTIMIZATION

4.1   Analysis and Modeling

The CFD analyses are performed using a custom version of NASA's FUN3D v13.2 with body-force modeling[4,10] and SWIFT v4.0[8] for the three-dimensional body-fitted aerodynamic analysis of turbomachines. The unstructured mesh for all the PAI models are generated by using Pointwise v18.02R2, and the turbo-machinery blade meshes are generated by using TCgrid v4.0[8]. The turbulence model for PAI model, i.e. FUN3D[10], is the Spallart Allmaras model without wall functions and the y+ of the presented cases are kept below 10, while the turbo-machinery CFD adopts Wilcox' *k-w* turbulence model. The actuator disk model is applied to get the initial condition for the body-force analysis.

4.2   Design Optimization with Axisymmetric Profile

4.2.1   Design Formulation

Maximize: η_{ad} (13)

Subject to: $C_1 = 0.5 - \frac{|\dot{m}-\dot{m}_0|}{\dot{m}_0} \times 100\ (\%) \geq 0.0$ (14)

$C_2^* = 0.5 - \frac{|Pr - Pr_0|}{Pr_0} \times 100\ (\%)$ (*only for front Rotor) (15)

$C_2^{**} = 1.0 - |\alpha - \alpha_0| \geq 0.0°$ (**only for rear Rotor) (16)

The flow-path geometry from the inlet to the nozzle is frozen and is kept the same as the conceptual one [5] because the current study only focuses on the preliminary design

of the blades. The number of design parameters for each rotor blade is 25 mean-line angle parameters i.e. 5 sections defined at 0%, 25%, 50%, 75%, 100% span and 5 per each section. Also, the metal chord lengths for 5 design sections which are evenly distributed radially from hub to tip. The stacking axis is automatically updated as the blade shape changes. The objective of the rotor design is to maximize the adiabatic efficiency, η_{ad}. The design cost function and constraints on fan pressure ratio, mass flow rate and exit flow angle are described in Eqs. (13)~(16), respectively. The design fan pressure ratio is set as the design condition and kept within 0.5% band during the optimization. The target mass flow rate is $\dot{m}_0$ and constrained also within 0.5% of variation. As indicated in Eqs. (14)~(16), the positive constraint values indicate that the design satisfies the imposed constraint during the optimization.
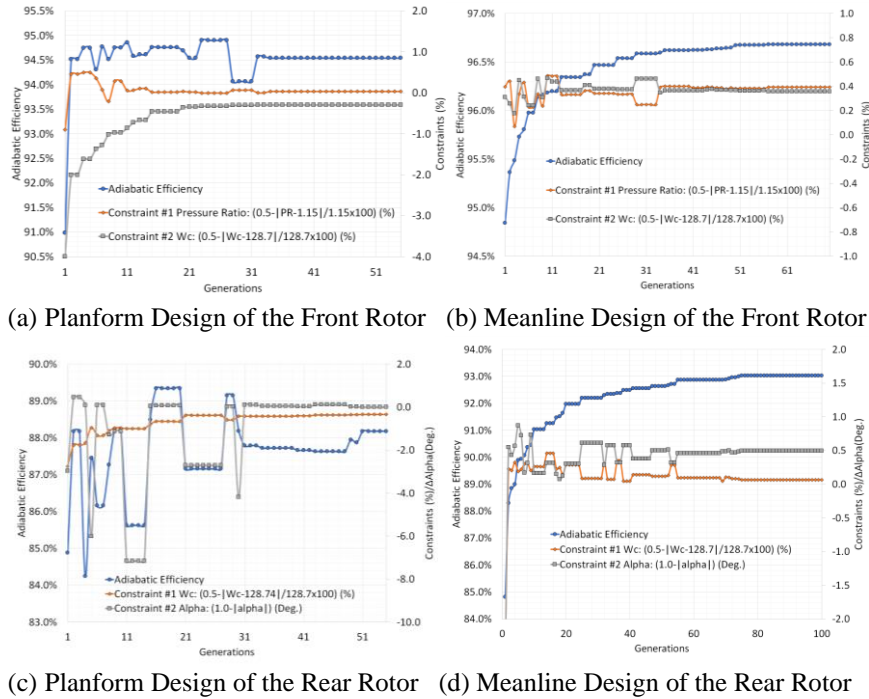

| (a) Planform Design of the Front Rotor | (b) Meanline Design of the Front Rotor |

| (c) Planform Design of the Rear Rotor | (d) Meanline Design of the Rear Rotor |

Figure 15. Design History of a pair of Counter Rotating Rotors (Examples).
[Front Rotor Design Condition: W_c = 128.7 kg/sec, N_c = 4000 RPM, PR_0 = 1.15, Rear Rotor Design Condition: W_c = 128.7 kg/sec, N_c = 4159 RPM, α_4 = 0°]

4.2.2   Optimized Blade Geometry

The shape optimizations of the rotor blades are performed for the axisymmetric inlet profile on single blade row CFD models. The blades are designed for the target condition as above-discussed. The inlet profile discussed in section 2.2 is applied to each category respectively. Figures 15 show examples of the design histories of the front and rear rotors with NSGA-II. In the history in the figures, the planform design in Figs. 15-(a) and (c) show the trade-off between the efficiency gains and meeting the constraints of the corrected flow rate and pressure ratio for (a), or the corrected flow rate and exit flow angles for (c). The meanline designs in Figs. 15-(b) and (d) show significant improvement in the efficiency as it starts from the baseline which already satisfies the constraints. The efficiency gain of the front rotor through the optimization process is about +6.6% from the baseline to the final blade from the meanline design as the design space includes enough design space to meet the constraints. On the other hand, the rear rotor design struggled with meeting the mass flow rate condition as well as exit flow angle at the same time. Thus, the efficiency gain is not as high as the front rotor could reach. However, still the adiabatic efficiency of the rear rotor achieves around 93% with fan pressure ratio of 1.14. The overall stage efficiency of the current design presented in Figs.14 is about 95%, stage pressure ratio is 1.31 at the design mass flow rate condition.

Figure 16 shows maps of the optimum solutions in different operating conditions. The best results of CRFs optimization at various rotational speed and maximum mass flow

rate conditions near the peak efficiency achievable for each design speed is presented in the figures. The blade count for each rotor design is adjusted to accommodate moderate range of the solidity that can allow the design mass flow rate. Even though the solidity is adjusted, the rear rotor easily stuck with the mass flow limit that is lower than the design requirements for slower speeds lower than 4000 RPM for 11 blade counts, and lower than 5000 RPM for 15 counts. Thus, the indicated mass flow rate conditions by red color in Fig. 16-(b) represent the maximum mass flow rates that the optimal design for each design speed could reach but violate the constraints. Consequently, the optimal number of the blade counts to satisfy the design goals simultaneously with good efficiency could be found through the parametric optimization processes. The front rotor with FPR =1.147, N_c=4200 RPM, W_c=128.7kg/sec, 19cnts and the rear rotor with FPR=1.142, N_c=4160 RPM, W_c=128.96kg/sec, 11cnts are chosen for the final blade designs. In addition, the chosen CRFs set is applied to re-evaluating new inlet profiles with body-force in PAI model.
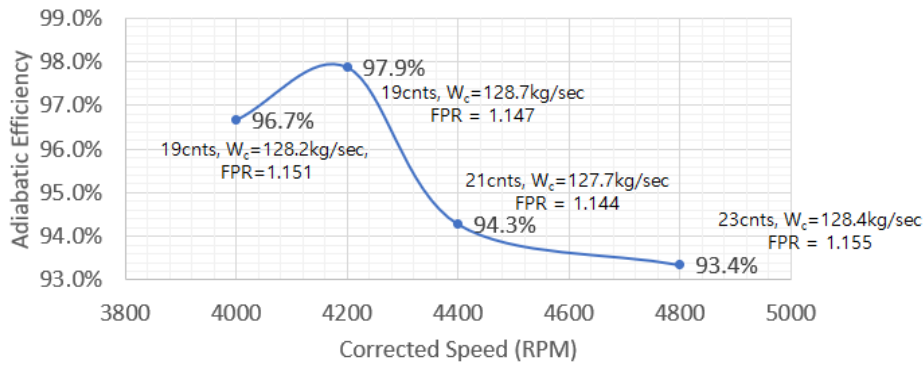
(a) Optimal Efficiency of the Front Rotor Designs per Rotational Speed
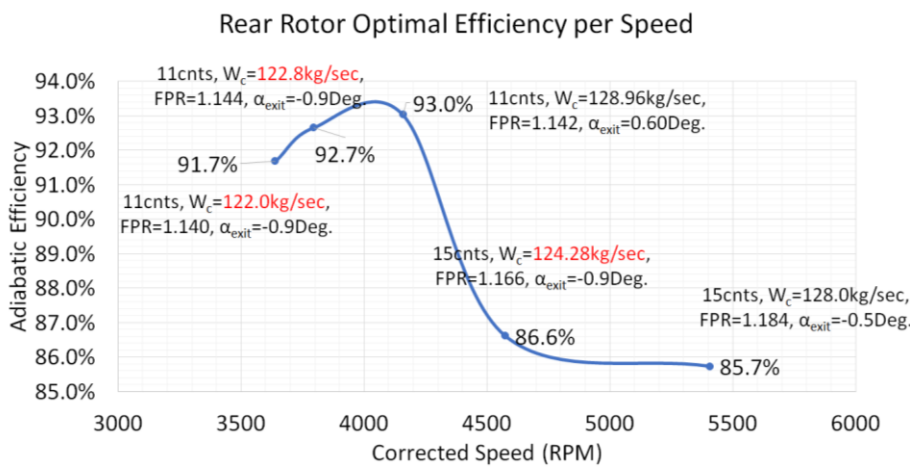
(b) Optimal Efficiency of the Rear Rotor Designs per Rotational Speed
Figure 16. Performance Map of Optimum CRF system designs.
[Slot 1 Axisymmetric Profile]

As mentioned before, the mass flow condition is critical for the shaft power and thrust estimation, thus, an appropriate planform shape should be found for each condition before the actual design of the meanline distributions. Figure 17 displays the history of the front rotor. From Fig. 17-(a), a raw fan design from the quasi-2D meanline code shows a significant separation on the suction side over almost whole span as seen in the upper plot that presents the axial negative velocity ISO contours. Plotted below is the corresponding axial momentum contour in the blade to blade view at the 50% span and again indicates the separation starts after 50% chord to trailing edge. Fig. 17-(b) is the best design from the planform design in which the design iterations are focused on satisfying the mass flow rate and pressure ratio constraints rather than improving the efficiency as shown in Fig. 15-(a). As the design constraints are satisfied from the planform design, the meanline

design from Fig. 17-(b) to Fig. 17-(c) shows a remarkable improvement in the efficiency and most of the trailing edge separation could be removed through the optimization.

The design of the rear rotor has different requirements. It is not targeting for the pressure ratio but the exit flow angles as defined in Eq. (16), and mass flow rate constraints in Eq.(14), so that the optimization would not be over-constrained to reach the optimum efficiency with the critical constraints satisfied. Similarly, Figs. 18 present a significant efficiency improvement from the baseline design to the optimized rotor design by removing the TE separation. The number of the blades of the rear rotor has been adjusted from 15 to 11 to accommodate the mass flow rate requirements based on the performance map in Fig. 16-(b).

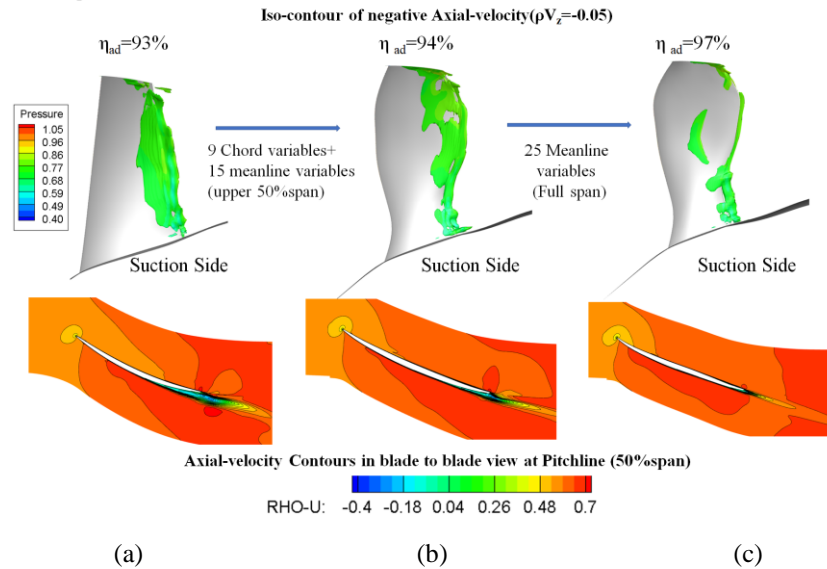(a)   (b)   (c)

Figure 17. Evolution of Design Optimization of the Front Rotor
[Target FPR = 1.15, N_c=4000 RPM, W_c=128.7 kg/sec, Upper row: ISO contours of negative axial velocity, Lower row: axial momentum contours at the pitch-line of the blade at 50% span]
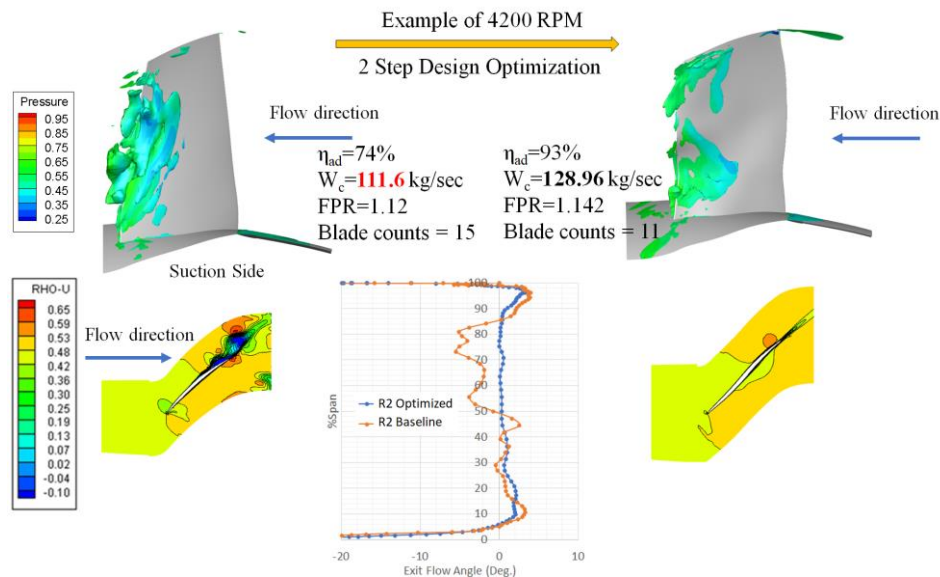

Figure 18. Design Optimization of the Rear Rotor
[Target: Exit Flow Angle < 0.5°, N_c = 4160 RPM, W_c = 128.7 kg/sec]

5.0   PERFORMANCE ASSESSMENT

5.1   New Inlet Profile

The optimized CRFs are applied to the PAI CFD model in the body-force form as shown in Figs. 19. The correction factors are obtained from the multi-stage CFD with axisymmetric inlet profile. It is noted that the inlet and exit profiles are fundamentally different from the distortion patterns predicted by the actuator disk model in Figs. 5. Two reasons for the differences in the flow pattern can be explained as follows; (1) The difference in radial work profile (AD model has a radially constant work profile) causes static pressure variation along the radial direction, thus, the ingested mass flow rate obtained from the body-force model could be changed; (2) The body-force model includes the consideration of the swirl effect. The circumferential mixing from the inclusion of the swirl of the fans, thus, generates more uniform flow at the exit than the AD model does.

Hence, the performances of the optimized CRFs are evaluated for the new inlet profiles captured from the results of the body-force model. Mass averaged performance from the 6 sectorial inlet profiles is compared with the performance from the axisymmetric profile in the following sub-section. In addition, the optimized CRFs is compared with a conventional reference high speed fan, R4, which is analyzed at the peak efficiency point of 87% of the design corrected speed for the design mass flow rate condition of the CRFs. In other words, the rotational speed of R4 fan is determined based on the target corrected flow of CRFs design (W_c=128.7kg/sec) to understand the advantage of the CRFs in the boundary layer ingesting propulsion.

The inlet profiles per sector in terms of the flow angle and total pressure ratio for the same slot (slot 1) in Figs. 20. The axisymmetric profile is also plotted for the comparison. As shown in Fig.20-(a), the swing of the inlet flow angle gets larger than those in Fig. 6-(b), i.e., $\pm15°$ at 50%span and $\pm25°$ at the hub. However, the swing at the tip is significantly reduced and the symmetricity with respect to center plane still exists. Thus, the axisymmetric profile shows about 5° reduction of the tip swirl as a result.

The current design is performed with the circumferentially averaged axisymmetric inlet profile which has almost no swirl due to the symmetricity of the profiles. However, the rotors will still go through a significant incidence swing per 1 revolution. Thus, the incidence tolerance may not be able to achieved by the adjustment of the incidence unless the distortion itself could be reduced by the refinement in airframe, inlet designs that precondition the upstream flow toward the fan face. However, the sensitivity for the distortion could be still mitigated by the rotor design itself such as the blunt leading edge and low tip speed designs.
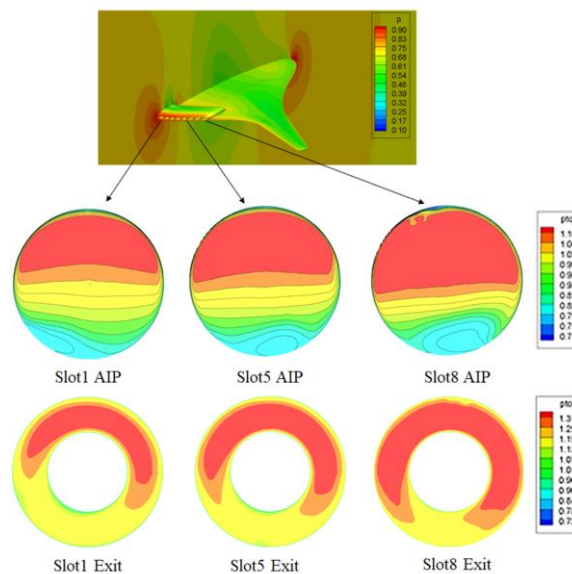

Figure 19. PAI CFD analysis at the cruise condition with body-force model from the optimized CRFs. (Th$_0$=80kN)

5.2   Multi-Stage CFD

To demonstrate the distortion tolerant characteristics of the low speed low pressure CRFs, a multi-stage CFD model for optimized CRFs is applied to 7 inlet profiles which include 6 sectorial and one axisymmetric inlet profiles. The results from the local sectors are circumferentially mass-weighted averaged to be compared with the axisymmetric profile. A conventional high-speed R4[12] fan, as a reference for the same 7 inlet profiles, is analyzed to investigate the capability of the designed CRFs in terms of the incidence tolerance. The exit boundary condition specifies the hub static pressure at the same pressure level as the axisymmetric profile case with radial equilibrium for each case instead of specifying the mass flow rate condition.

Figures 21 show the Mach number contours at the tip (90% span), pitch-line (50% span) and hub (10%) for the axisymmetric profile case. Same contours from the R4 fan at 6013 RPM (87% N_c) are compared. The corrected mass flow rate for both cases are set as W_c=270 (lbm/sec). Note that a corrected speed that pumps the same amount of the design mass flow rate as the CRFs' is found as the high-speed fan is not designed (or optimized) for the boundary layer ingesting profile, thus, the pressure ratio through the high fan (FPR=1.22) is found lower than that of CRFs (FPR=1.31).

Although the CRFs are designed for the inlet profile from actuator disk model, the fans are working reasonably well with the new inlet profile. The leading edge of the rear rotor goes through small shock on the suction side at the tip and the mid-span region but the loss associated with those is relatively lower and locally confined in a passage compared with that of the high-speed fan. Overall, both CRFs and high-speed fan operate in a good working condition. The CRFs achieved 94% adiabatic efficiency for FSPR=1.31 and R4 reached 90.3% for FPR=1.22 for the given mass flow rate condition. The hub contour of the high-speed fan indicates that the hub area almost reaches the choking condition near the trailing-edge region.

A normalized total pressure contours from two extreme inlet conditions, i.e., sector 1(near choking condition) and 5 (largest incidence at the tip, thus, near stall condition) profiles are compared in Figs. 22 and 23. Since the fan pressure ratio of the two different fans are not same, the total pressure contours are normalized with respect to the 1-D face averaged pressure at the fan exit from the axisymmetric profile. Figs. 22 are presenting the comparison at the sector 1 inlet profile while Figs. 23 are those from sector 5 profile.
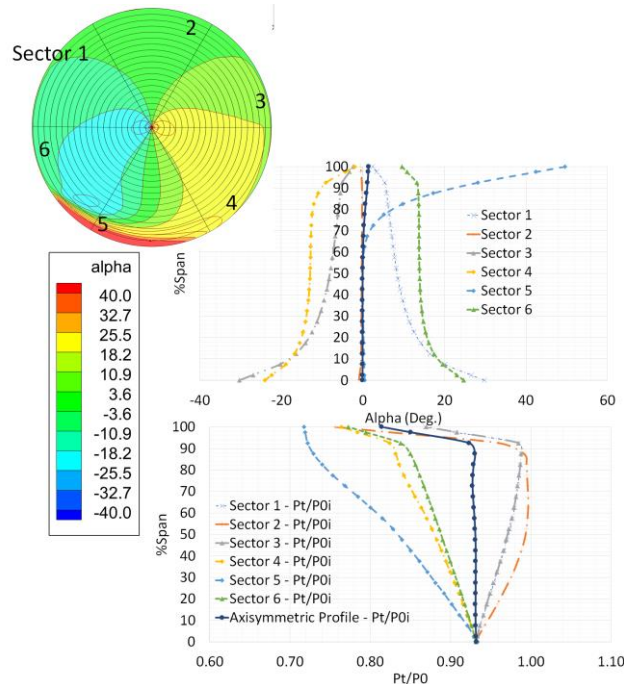
(a) Inlet Flow Angle (Upper), (b) Total Pressure Profiles (Lower)
Fig. 20. Inlet Profiles from PAI CFD model with the body-force model[4] including swirling effects. (Slot 1, Th_0=80kN)

(a) Axisymmetric profile, 90%Span (Left: CRFs, Right: High-Speed Rotor (R4))

(b) Axi-Symmetric, 50%Span (Left: CRFs, Right: High-Speed Rotor (R4))

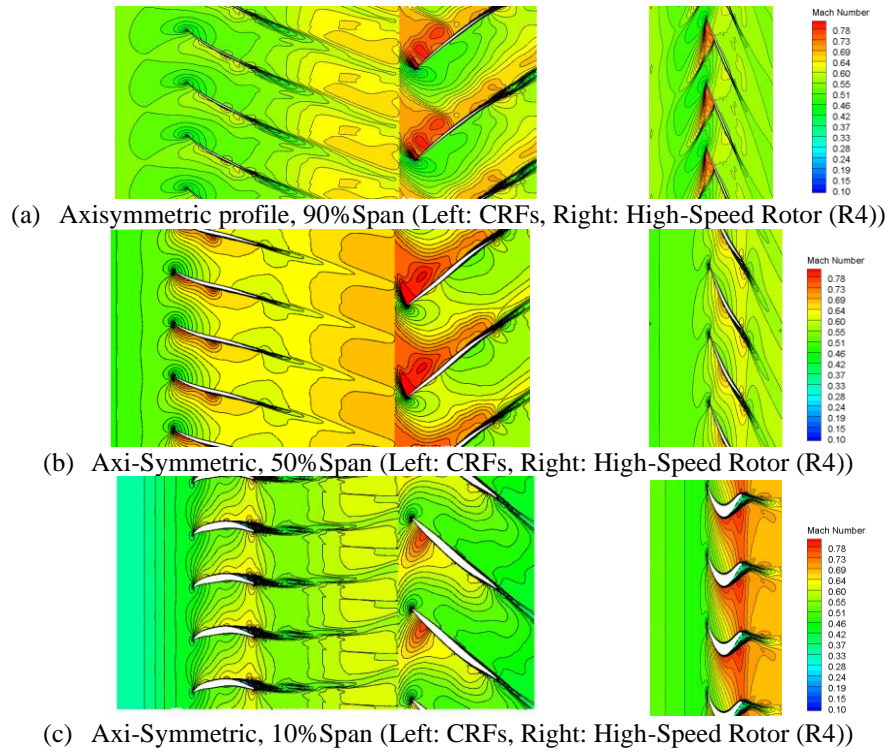(c) Axi-Symmetric, 10%Span (Left: CRFs, Right: High-Speed Rotor (R4))

Fig. 21. Mach number contours at select blade sections of CRFs and high-speed rotor for axisymmetric inlet profile [z-θ plane in cylindrical coordinate, N_{c1}=4200RPM, N_{c2}=4159RPM, $N_{c,HS}$=6013.4 RPM, $\eta_{poly,CRF}$=94%, $FSPR_{CRF}$=1.31, $\eta_{poly,HS}$=90.3%, FPR_{HS}=1.22]

(a) Sector 1, 90%Span (Left: CRFs, Right: R4 HS fan)

(b) Sector 1, 50%Span (Left: CRFs, Right: R4 HS fan)

(c) Sector 1, 10%Span (Left: CRFs, Right: R4 HS fan)
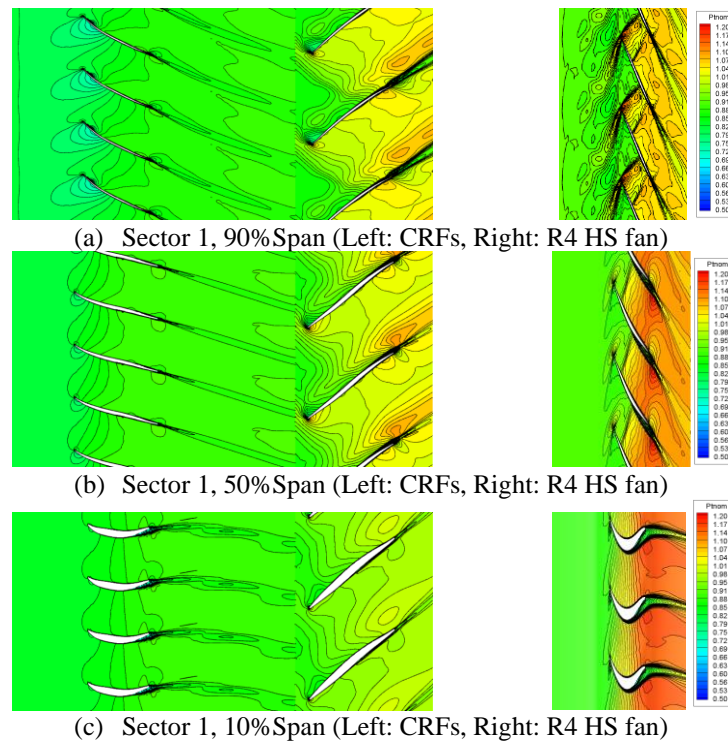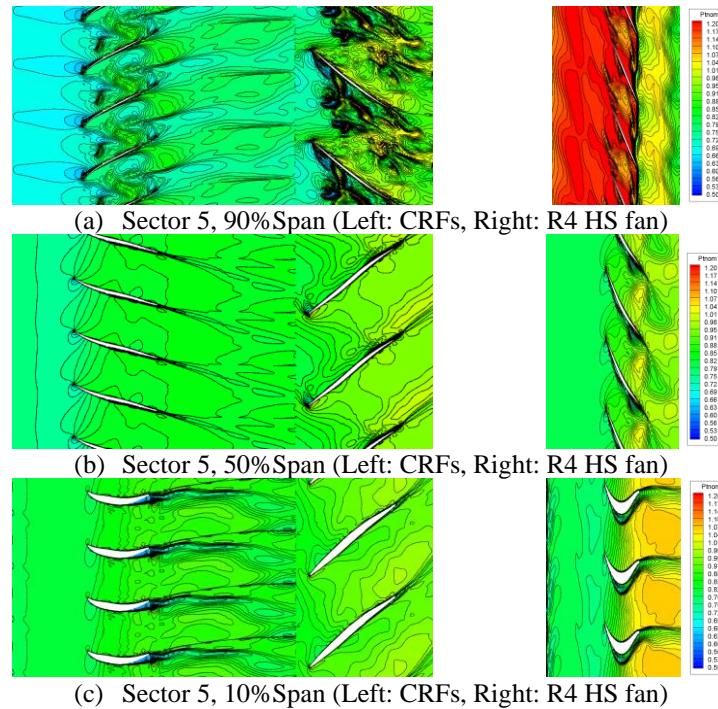
Fig. 22. Normalized total pressure contours at blade-to-blade sections [z-θ plane in cylindrical coordinate, N_{c1}=4200RPM, N_{c2}=4159RPM, $N_{c,HS}$=6013.4RPM, $\eta_{poly,CRF}$=92.5%, $FSPR_{CRF}$=1.25, $\eta_{poly,HS}$=89.2%, FPR_{HS}=1.16]

(a)   Sector 5, 90%Span (Left: CRFs, Right: R4 HS fan)

(b)   Sector 5, 50%Span (Left: CRFs, Right: R4 HS fan)

(c)   Sector 5, 10%Span (Left: CRFs, Right: R4 HS fan)

Fig. 23. Normalized total pressure contours at blade-to-blade sections [z-θ plane in cylindrical coordinate, N_{c1}=4200RPM, N_{c2}=4159RPM, $N_{c,HS}$=6013.4RPM, $\eta_{poly,CRF}$=85.8%, FSPR$_{CRF}$=1.33, $\eta_{poly,HS}$=N/A[*], FPR$_{HS}$=1.13, *note that high speed fan results are not fully converged solution due to the stall inception, only for a qualitative comparison]

A stall inception and significant reverse flow are observed at the tip of the high-speed fan in Fig.23.-(a, Right). The contour of the counter rotating fan in Fig. 23.-(a, Left) also indicates that the running condition is near stall as the flows on the suction sides of both front and rear rotors separate. However, the mid-span and hub contours reveals that the separation bubble from the CRFs are confined locally at the tip, while the stall expands to the mid-span in the high-speed fan solution. Further investigation of the distortion tolerance from the rotational speed is made by the total pressure contours from the rotor exits in Figs. 24. The contours are normalized by the predicted exit pressure (face-averaged) of the stage from the axisymmetric case. Fig. 24.-(a) presents the total pressure contour at the exit of the front rotor (FPR=1.15) and Fig. 24.-(b) depicts the exit contour of the high-speed rotor (FPR=1.22).

Tip separation is observed not only in sector 5 but also in sectors 2, 3 and 4 but the loss from the separation is limited at the very shroud area and circumferentially spread in Fig. 24.-(a). On the other hand, the loss from tip separation of the high speed fan rather extends to the radial direction than the circumferential direction in Fig. 24.-(b). In addition, the variation of the profile loss (wake loss) from the high speed fan cases are more eminent. The overall trend is that the high-speed fan shows more profile loss from the incidence swing. However, the low speed fan shows worse end wall characteristics though the loss from the end wall seems to be confined in the radial direction. Thus, the stall inception could be delayed and the loss variation among the sectors due to the distortion could be minimized. The circumferential variation of the total pressure among the sectors reduced fundamentally through the rear rotor as shown in Fig. 24.-(c). Especially, the end-wall flow from the sectors 4 and 5 of which total pressure were significantly lower than the face averaged value at the exit of the front rotor in Fig. 24.-(a) obtained more propulsive energy from the second rotor compared with other sectors. Thus, the radial variation of the pressure profile at the stage exit got remarkably more uniform than that of the high-speed fan results.

(a) CRFs – Front Rotor Exit
(Normalized by FPR=1.15)

(b) HS Fan (R4) Exit
(Normalized by FPR=1.22)

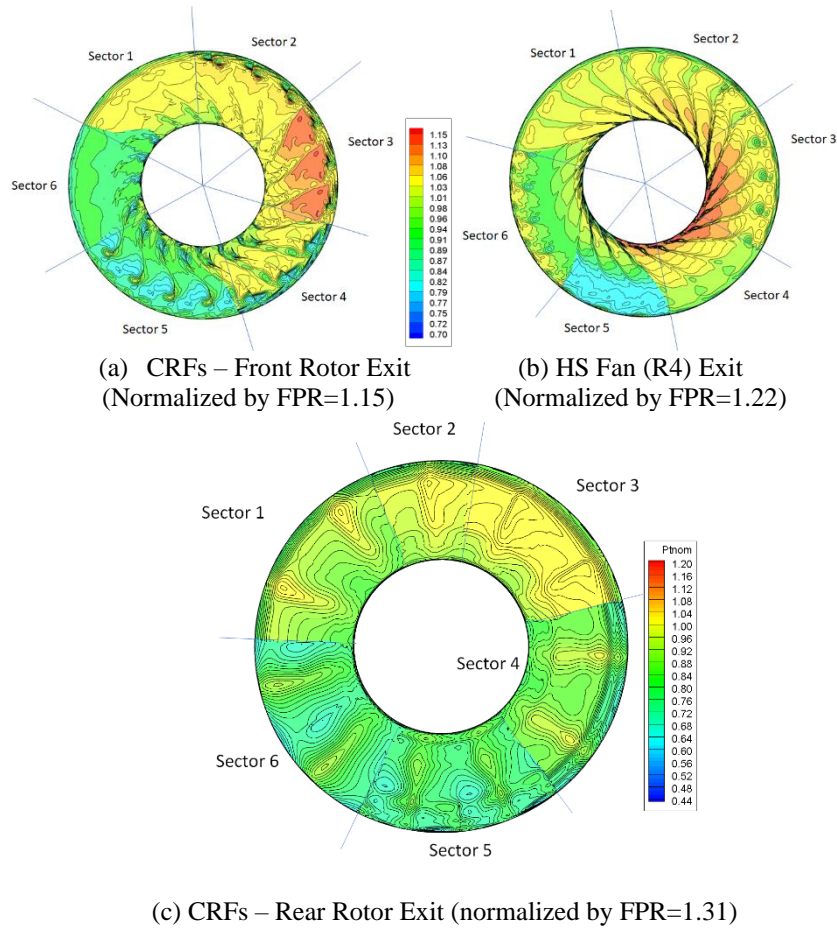(c) CRFs – Rear Rotor Exit (normalized by FPR=1.31)

Fig. 24. Comparison of Normalized Total pressure Contours at the stage exit
from the 6 sectors.

5.3   Performance Comparison

The performance metrics are compared for the cases analyzed in the previous chapter. The polytropic efficiency of both front and rear rotors and the stage from each sectorial and axisymmetric profiles are compared with each other and high speed R4 fan. For a reference, a mass averaged efficiency of all the 6 sectors are evaluated as well. The axisymmetric profile for which the rotors are designed in terms of inlet flow swirl - 0 deg. except the inclusion of sector 5 tip region - shows quite optimistic, better results even than the best efficiency case among all the sectors. On the other hand, the mass weighted average value indicates the fan stage efficiency is estimated about 88%. The high-speed fan shows similar reaction to the characteristics of the first rotor of the CRFs against the sectorial inlet profiles. However, an efficiency offset of 3~4% between low and high speed fans is observed. Interestingly, the stage efficiency of the CRFs shows less sensitivity to the inlet profiles while each rotor still shows sensitivity level similar to the high-speed fan. That is interpreted that the front and rear rotors work complementarily compensate each other's deficiency, thus, the rear rotor works more efficiently when the front rotor works less efficiently and vice versa. Hence, this complementary characteristics of CRFs introduces a high distortion tolerance capability compared with the conventional fan-OGV systems.
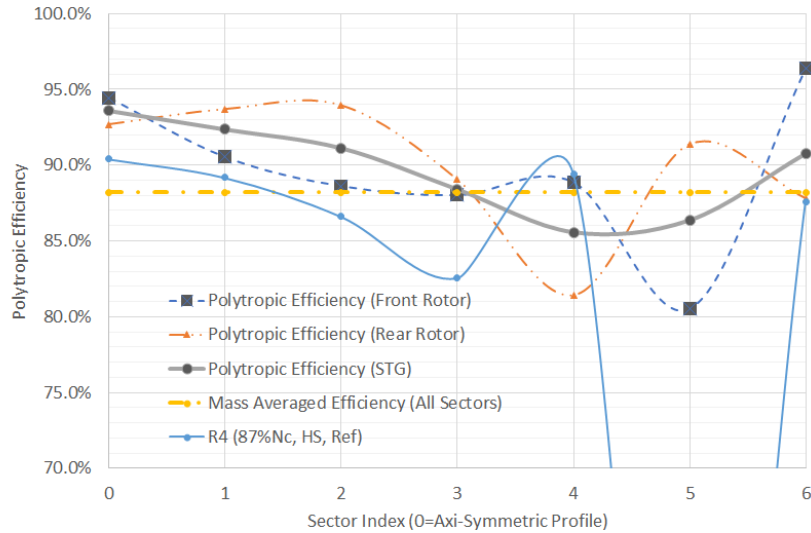
Fig. 25. Comparison of polytropic efficiency of front/rear rotors and stage from 6 sectors and axisymmetric inlet profiles.

Similar conclusion could be drawn from the comparison of the total pressure ratio in Fig. 26. For the sectors 1~3 and 6, the offset of the pressure ratio between the first rotor of CRFs and high-speed fan is almost constant. However, the high-speed fan shows much more drastic change in its reaction against the sector 4 and 5 profiles where the stall starts incepting. Thus, it could be read that the low speed concept of each rotor of the CRFs brings in higher stall margin and benign choking for both side of the speed line. Especially, the complimentary reaction of the two rotors makes the propulsor operate more tolerantly under the circumferential distortion as shown in the sector 5 performance.

The shaft-power estimation in terms of the total temperature ratio in Fig. 27 shows that the over- and under-shoot of the power on the high-speed fan under sector 5 and 6 profiles are mitigated by the counter rotating fan operation. The overall temperature ratio variation of the stage of the CRFs has much smaller amplitude than that of the high-speed fan as well.
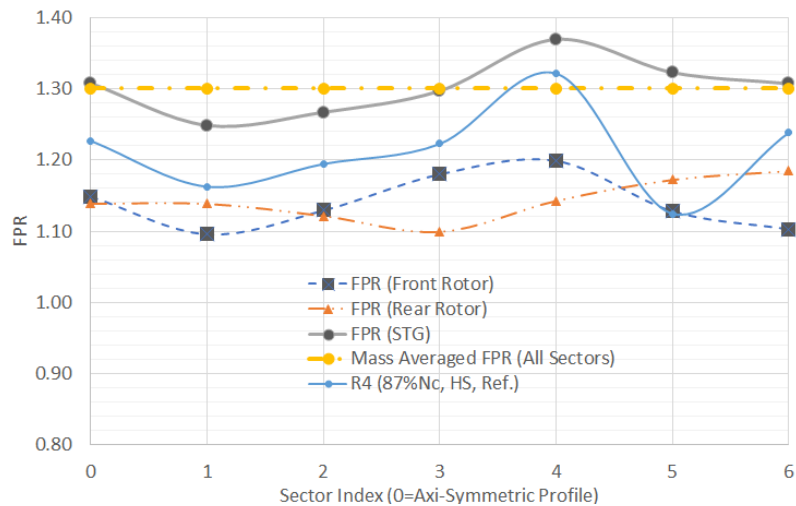

Fig. 26. Comparison of Total Pressure Ratio of Front/Rear Rotors and Stage from 6 sectors and axisymmetric inlet profiles.
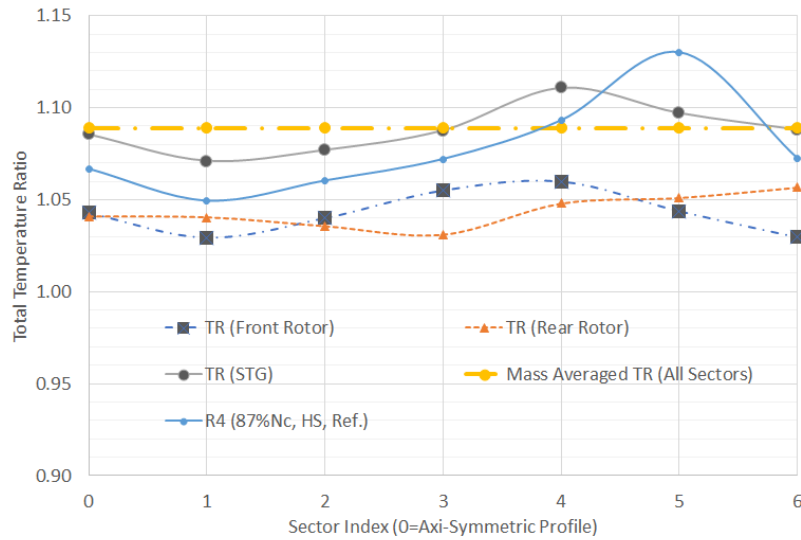
Fig. 27. Comparison of Total Temperature Ratio of Front/Rear Rotors and Stage from 6 sectors and axisymmetric inlet profiles.

CONCLUDING REMARKS

A distributed and embedded low speed/low pressure ratio CRFs is conceptually designed. A close to 20% fuel saving benefit is realized with the help of the multi-objective optimization. The design goal is to maximize the fan efficiency with low sensitivity against the incoming swirl distortion from the boundary layer ingestion, i.e., seeking propulsor design with distortion tolerance characteristics. Aerodynamic optimization of multiple objectives including the fan adiabatic efficiency, target mass flow rate, pressure ratio, and the exit flow angle of the fan stage are sequentially carried out by using a genetic algorithm. Multiple optimum solutions for various rotational speed, the speed ratio of the two rotors, and blade counts are obtained within the guidelines of the diffusion factor and flow capacity from the velocity vector study and quasi-2D meanline model. The performance of the optimized CRFs in an embedded mail-slot nacelle is evaluated from the perspective of a loosely coupled propulsion airframe integration, basing on six selected circumferentially averaged sectorial inlet profiles and their axisymmetric averaged profile. The performance is compared with a conventional high-speed fan (R4) for the same conditions. It is found that low blade loading per rotor enables higher efficiency achievement than that of the high-speed fan. Also, the corresponding low rotational speed made the stall and choking characteristics of the fan stage less sensitive to the condition, hence, the circumferential distortion tolerance could be achieved. Finally, it is also found that the counter rotating rotors are working in a complimentary way for each other, thus, the overall stage performance could be less sensitive to the inlet conditions from the efficiency penalizing boundary layer ingestion.

ACKNOWLEDGMENTS

REFERENCES

[1] FELDER, J., KIM, H.D., AND BROWN, G.V., "AN EXAMINATION OF THE EFFECTS OF BOUNDARY LAYER INGESTION ON TURBOELECTRIC DISTRIBUTED PROPULSION SYSTEMS," AIAA2011-300, 2011.

[2] KIM, H., HARDING, D., GRONSTAL, D. T., LIOU, M.-F., AND LIOU, M.-S.: AERODYNAMIC DESIGN OF HYBRID WINGBODY WITH NACELLE: N3–X PROPULSION-AIRFRAME CONFIGURATION. AIAA 2016–3875, 2016. HTTPS://DOI.ORG/10.2514/6.2016-3875

[3] KIM, H., LIOU, M.-F. AND LIOU, M.-S. "MAIL-SLOT NACELLE SHAPE DESIGN FOR N3-X HYBRID WING BODY CONFIGURATION," AIAA 2015-3805, AIAA PROPULSION & ENERGY FORUM 2015, ORLANDO, FL, 27-29 JULY 2015.

[4] KIM, H., AND LIOU, M.-S. "FLOW SIMULATION AND OPTIMAL SHAPE DESIGN OF N3-X HYBRID WING BODY CONFIGURATION USING A BODY FORCE METHOD," AEROSPACE SCIENCE AND TECHNOLOGY, VOL. 71, PP. 661-674, OCT., 2017.

[5] LEE, B., LIOU, M. AND KIM, H., "AERODYNAMIC CONCEPTUAL DESIGN OF BOUNDARY LAYER INGESTION PROPULSOR SYSTEMS: HYBRID WINGBODY AIRCRAFT WITH PROPULSION-AIRFRAME-INTEGRATION," AIAA2018-3954, 2018.

[6] LIOU, M.-F., KIM, H.J., LEE, B.J. AND LIOU, M.-S., "AERODYNAMIC DESIGN OF INTEGRATED PROPULSION-AIRFRAME CONFIGURATION OF THE HYBRID WINGBODY AIRCRAFT," AIAA 2017-3411, 35TH AIAA APPLIED AERODYNAMICS CONFERENCE, JUNE 05-09, 2017, DENVER, CO, 10.2514/6.2017-3411.

[7] LEE, B., AND LIOU, M.-F.,"AERODYNAMIC DESIGN AND OPTIMIZATION OF FAN STAGE FOR BOUNDARY LAYER INGESTION PROPULSION SYSEM," ICCFD10-091, 2018.

[8] CHIMA, R. V., "A THREE-DIMENSIONAL UNSTEADY CFD MODEL OF COMPRESSOR STABILITY," GT2006-90040, 2006.

[9] DEB, K., PRATAP, A. AGARWAL, S. AND MEYARIVAN, T., "A FAST AND ELITIST MULTIOBJECTIVE GENETIC ALGORITHM: NSGA-II," IEEE TRANSACTIONS ON EVOLUTIONARY COMPUTATION, VOL.6, NO.2, APR. 2002.

[10] BIEDRON, R., CARLSON, J., DERLAGA, J., GNOFFO, P., HAMMOND, D., JONES, W., KLEB, B., LEE-RAUSCH, E., NIELSEN, E., PARK, M., RUMSEY, C., THOMAS, J. AND WOOD, W., " FUN3D MANUAL: 13.3," NASA/TM-2018-219808.

[11] AREND, D., "EXPERIMENTAL EVALUATION OF EMBEDDED BOUNDARY LAYER INGESTING PROPULSOR FOR HIGHLY EFFICIENT SUBSONIC CRUISE AIRCRAFT," AIAA 2017-5041

[12] SMITH, L. H., "WAKE INGESTION PROPULSION BENEFIT," J. PROPULSION AND POWER, VOL. 9, 74-82, 1993.

[13] HUGHES, C. E., "AERODYNAMIC PERFORMANCE OF SCALE-MODEL TURBOFAN OUTLET GUIDE VANES DESIGNED FOR LOW NOISE," AIAA-2002-0374, AIAA, 2002. ALSO NASA/TM-2001-211352, 2011.

[14] LEE, B., LIOU, M.-F. AND LIOU, M.-S., "CONCEPTUAL DESIGN OF A TAIL-CONE THRUSTER SYSTEM UNDER AXI-SYMMETRIC INLET DISTORTION," GT2018-75861, 2018.

[15] RONALD H. AUNGIER, "AXIAL-FLOW COMPRESSORS", ASME EDUCATIONAL SERIES, PUBLISHED: 2003, DOI:10.1115/1.801926 0